NANO LETTERS
Letter
pubs.acs.org/NanoLett

Optical Forging of Graphene into Three-Dimensional Shapes

Andreas Johansson,[†,‡] Pasi Myllyperkiö,[†] Pekka Koskinen,[‡] Jukka Aumanen,[†] Juha Koivistoinen,[†] Hung-Chieh Tsai,[§] Chia-Hao Chen,[∥] Lo-Yueh Chang,[∥] Vesa-Matti Hiltunen,[‡] Jyrki J. Manninen,[‡] Wei Yen Woon,[§] and Mika Pettersson*,[†]

[†]Nanoscience Center, Department of Chemistry, [‡]Nanoscience Center, Department of Physics, University of Jyväskylä, P.O. Box 35, FI-40014 Jyväskylä, Finland

[§]Department of Physics, National Central University, Jungli, 32054, Taiwan, Republic of China

[∥]National Synchrotron Radiation Research Center, Hsinchu, 30076, Taiwan, Republic of China

Supporting Information

ABSTRACT: Atomically thin materials, such as graphene, are the ultimate building blocks for nanoscale devices. But although their synthesis and handling today are routine, all efforts thus far have been restricted to flat natural geometries, since the means to control their three-dimensional (3D) morphology has remained elusive. Here we show that, just as a blacksmith uses a hammer to forge a metal sheet into 3D shapes, a pulsed laser beam can forge a graphene sheet into controlled 3D shapes in the nanoscale. The forging mechanism is based on laser-induced local expansion of graphene, as confirmed by computer simulations using thin sheet elasticity theory.

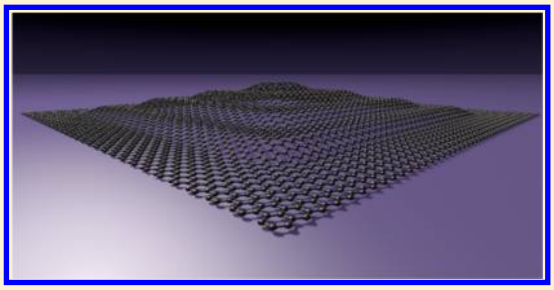

KEYWORDS: *Graphene, strain-engineering, femtosecond laser, defects, 3-dimensional, elasticity modeling*

Graphene, a single atomic layer of carbon, is the most studied 2D material and is characterized by excellent carrier mobility, strength, flexibility, transparency, and constant absorption in a broad range of the electromagnetic spectrum, making graphene an excellent material for novel applications in electronics, photonics, and optoelectronics.[1,2] Examples of reported devices include sensors, field effect transistors (FET), supercapacitors, and photodetectors.[3] Graphene is not strictly planar but contains corrugations, wrinkles, ripples, and other out-of-plane deformations.[4] These structural changes provide a way to modify the electronic properties of graphene, but controlling them is challenging.[5−8] So far, the modification of the third dimension of graphene has relied on spot-blistering, substrate molding, or strain-induced periodic modulation, as well as cutting graphene or connecting graphene flakes with functional groups, while controlled shaping of graphene itself into more complex custom-made 3D architectures has remained elusive.[9−13]

Here, we demonstrate the forging of graphene into free-standing 3D shapes by exploiting local strain induction due to irradiation with femtosecond laser pulses under inert atmosphere. While laser irradiation in air has earlier been shown to generate two-photon functionalization of the graphene surface with oxygen containing groups,[14] we argue here that the inert atmosphere allows a fundamentally different process of defect engineering to take place. Computer simulations using elasticity theory confirm experimental observations and provide the theoretical basis for the method. The optical forging opens new possibilities for fundamental studies and for the development of applications based on 3D shapes of graphene.

We patterned single-layer graphene on a Si/SiO$_2$ substrate by direct laser writing with tightly focused femtosecond pulses under nitrogen and argon atmospheres, which both produced qualitatively similar results. A matrix of $2 \times 2\ \mu\text{m}^2$ squares was patterned on graphene. Each square was irradiated by 441 partially overlapping spots at 100 nm spot separation. The irradiation time per spot was varied from 0.1 to 2.0 s. Surprisingly, the irradiated squares formed elevated flat plateaus with sharp boundaries, as seen in atomic force microscope (AFM) images (Figure 1a). The height varies from ~3 nm up to ~20 nm (Figure 1b) and is proportional to the square root of irradiation time (Supporting Information, Figure S1). This proportionality can be theoretically justified, as shown later. We did not observe any wrinkling on the plateaus or just outside them, except for folding already present in graphene before patterning. Remarkably, the patterned matrix is well visible under an optical microscope due to enhanced reflection of the irradiated areas (Figure 1c). With increasing irradiation time, the brightness of the irradiated spots increases, and the color changes from greenish toward yellow.

The squares are visible in a Raman map of the integrated intensity of the D-band including the contribution from the overlapping broad emission, which increases with irradiation

Received: August 17, 2017
Revised: September 12, 2017
Published: September 19, 2017

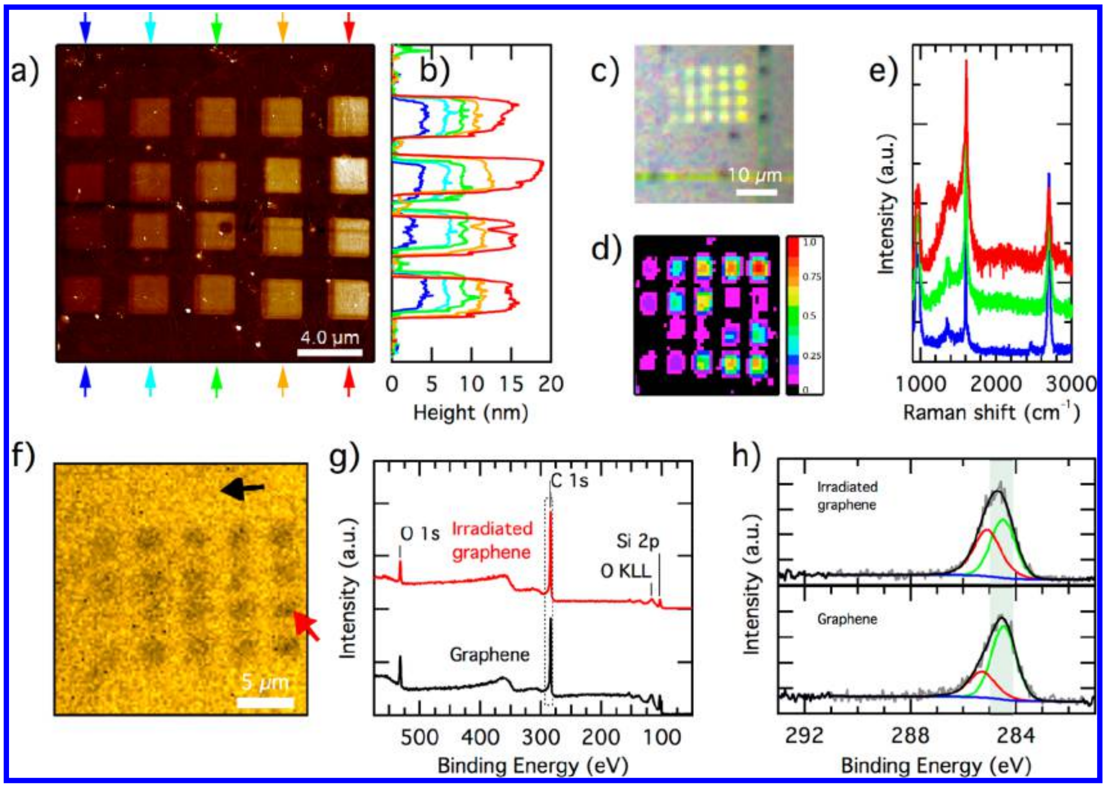

Figure 1. Characterization of irradiated graphene. (a) AFM image. (b) Line profiles of the AFM image between the arrows, shown in a. (c) Optical microscope image. The lines on the bottom and right are a part of the 30 nm thick and 1 μm wide gold reference grid. (d) Raman map showing integrated intensity in the D-band area at ~1350 cm^{-1}. (e) Raman spectra measured from graphene with no irradiation (bottom) and with 0.5 s (middle) and 2 s (top) of irradiation per spot. (f) XPS image of the C 1s signal at 285.0−284.2 eV. (g) XPS survey spectra of nonirradiated graphene (bottom) and irradiated graphene (top). (h) XPS C 1s spectra of nonirradiated area (bottom; black arrow in f) and irradiated area (top; red arrow in f). The shaded area shows the region used to construct the image in f. The gray line shows the raw spectrum; the black line is the fit that contains components of C═C (green), C−C (red), and background (blue).

(see Figures 1d and e). While local variations are observed, there is an overall trend toward increased integrated intensity with increased irradiation time. The characteristic spectrum of nonirradiated graphene (Figure 1e, bottom) is observed also in the irradiated areas (Figure 1e, middle and top). Note that the Raman spectrum of nonirradiated graphene does not show any significant presence of amorphous carbon, which excludes amorphous carbon redeposition or exfoliation[15] as the cause for the elevated plateaus. With increasing irradiation dose, broadened G- and D-bands develop, while the normal Raman spectrum of (nonirradiated) graphene remains (Figure 1e). The total spectrum is thus a sum of two components: normal and broad (additional Raman spectra are shown in Supporting Information, Figure S2). The broad spectrum resembles highly disordered graphene, but there is no growth of a sharp D-band, which is a characteristic signature of scattered point defects in graphene.[16,17] These observations suggest that irradiation transforms local regions of graphene into disordered form. In Raman spectra, also a broad emission background emerges upon irradiation (seen as a rising background in Figure 1e).

The sample was imaged by X-ray photoelectron spectroscopy (XPS) at submicrometer spatial resolution (Figure 1f). XPS did not reveal significant change in the chemical composition of graphene irradiated under nitrogen atmosphere (Figure 1g). Yet, contrast is found in scanning photoelectron microscopy due to overall lower XPS intensity for patterned areas (Figure 1f). The carbon C 1s peak becomes broader toward the higher binding energy tail, indicating a decrease in the sp^2 C═C bond and increase in the C−C bond density (Figure 1h). The XPS data are consistent with the defect generation picture as deduced from Raman spectra. The lack of oxygen containing groups again supports the notion that amorphous carbon does not contribute to the elevated plateaus. For comparison, irradiation of the same sample with analogous patterns under air reveals characteristic signals of oxidized carbon (Supporting Information, Figure S3).[14,18,19]

To further investigate the nature of the elevated plateaus we prepared a series of square patterns and compared them to square patterns made under air. In Figure 2a, two rows of squares patterned on graphene are presented. The barely visible top row was patterned under air, leading to functionalization of the surface with mainly epoxy and hydroxyl groups.[14,19] The height of the squares is about 1.3 nm. The bottom row was patterned under nitrogen, leading to elevated plateaus of about 20 nm in height. At the center of the image there is a triangular-shaped area in which the graphene has folded toward the upper right corner. In that area, no pattern is formed under either oxygen or nitrogen atmosphere, and the surface seems unaffected by the laser exposure. This observation again refutes that amorphous carbon deposition would contribute to the elevated plateaus. Additionally, it refutes the possibility of formation of elevated plateaus due to swelling of the underlying SiO_2 substrate.[20,21] Folds, cracks, and other surface features on graphene continue from the areas outside the plateaus to the inside. This is strong additional evidence that deposition of material cannot be responsible for the elevated features.

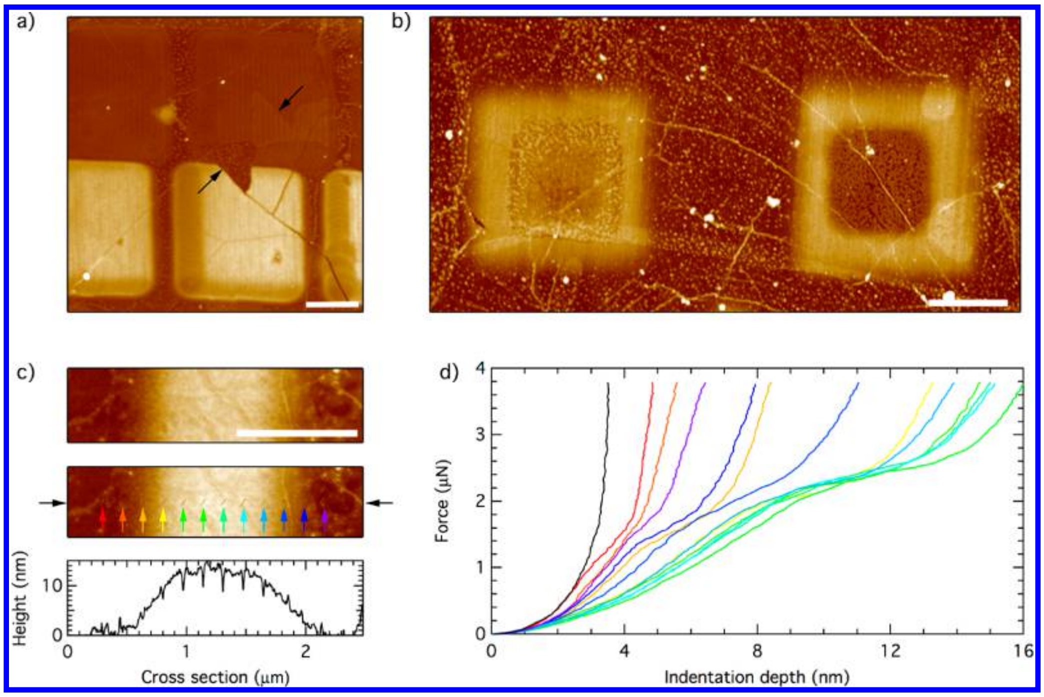

Figure 2. (a) AFM image of squares patterned under air (top) and nitrogen (bottom). The arrows point out where a triangular shaped section of graphene has folded. (b) AFM image of large squares patterned under nitrogen, with center regions in addition patterned under air. The center region was patterned after the larger square for the left pattern and before the larger square for the right pattern. (c) AFM data from nanoindentation area, showing topography before (top pane) and after (middle pane). The cross section (bottom pane) is taken between the black arrows in the middle pane. (d) Nanoindentation data showing the measured force versus indentation depth. The trace colors correspond to the arrow colors in c showing the measurement location, except for the black trace, which is measured on bare SiO_2. All scale bars are 1 um.

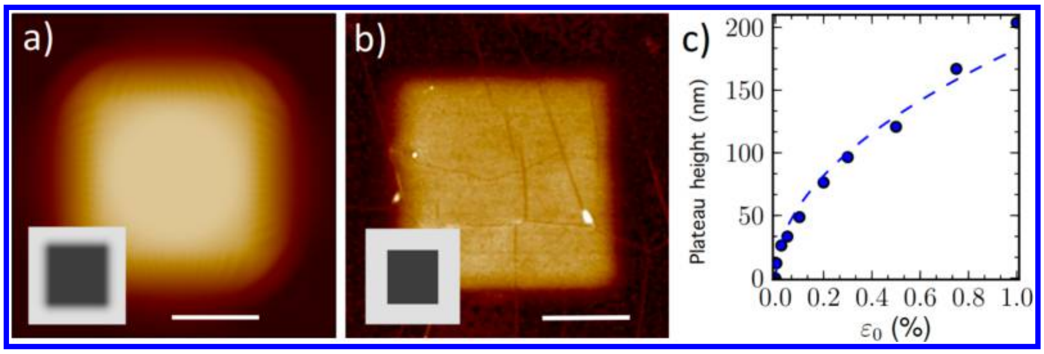

Figure 3. Elasticity modeling of plateau formation by local expansion. (a) Optimized topography of a simulated 2×2 μm^2 square pattern. Inset: the input strain field $\varepsilon(\mathbf{r})$; maximum strain is $\varepsilon_0 = 4.5 \times 10^{-5}$. (b) AFM topography of the plateau (corresponding to 1.5 s irradiation time in Figure 1a). The plateau height is 12 nm in both simulation and experiment. Inset: bitmap image used for laser writing. Scale bars, 1 μm. (c) Simulated height of 2×2 μm^2 square plateaus at different ε_0; the dashed line is eq 1.

Figure 2b shows two square patterns prepared by combining laser patterning under both air and nitrogen. For the left square pattern, first the large 2×2 μm^2 square was patterned under nitrogen, forming a 6 nm high plateau. Then the inner 1×1 μm^2 square was patterned under air. The inner square is somewhat crumpled with an average height of 3.5 nm. For the right square pattern, first the inner 1×1 μm^2 square was patterned under air and the outer 2×2 μm^2 square patterned under nitrogen. Here the inner square has a height of 1.3 nm, which is similar to oxidized areas in Figure 2a. The outer frame is again 6 nm high. The data show that functionalization of the graphene surface with oxygen containing groups leads to suppression of elevated plateau formation.

We also performed AFM nanoindentation across a 12 nm high, 1 μm wide, and 6 μm long graphene plateau. The nanoindentation area is shown in Figure 2c before (top) and after indentation (middle), together with a cross section (bottom) along the indentation line. The measured force versus indentation depth curves are shown in Figure 2d, with color corresponding to the arrows in Figure 2c pointing out their measurement locations. The resulting force versus indentation depth curves show initially a nonlinear increase, with a much weaker response than indentation on bare SiO_2 surface (black trace). At around 2 μN a plateau develops, which is interpreted as the graphene feature buckling toward the surface. It is interesting to note that this force is very similar to the nanoindentation force at which suspended graphene membranes break.[22,23] The force curve then increases again with a dependence similar to that of indentation on a bare SiO_2 surface. The onset of the second increase corresponds well to the height of the graphene structure, indicating that the onset corresponds to the tip reaching the SiO_2 surface. The AFM

DOI: 10.1021/acs.nanolett.7b03530
Nano Lett. 2017, 17, 6469−6474

image taken after nanoindentation (Figure 2c, middle) shows that the graphene structure has returned to its original shape, except for piercing marks where the AFM probe was indenting the surface.

All of the evidence taken together suggests that irradiation under inert atmosphere leads to the formation of elevated graphene structures containing only carbon. The most plausible explanation for the underlying driving force is that, by analogy to the blister formation in polymers, photons modify the lattice and induce local expansion of graphene.

To investigate this hypothesis, we used thin sheet elasticity theory to model expanded and deformed graphene (see Supporting Information). We assumed that, via a mechanism discussed later, the laser-induced lattice expansion field $\varepsilon(\mathbf{r})$ is proportional to the spatial irradiation dose $I(\mathbf{r})$. The spatial dependency was adopted from experimental input in conjunction with a Gaussian beam profile (full-width at half-maximum, fwhm = 500 nm).[18] The maximum strain $\varepsilon_0 = \max[\varepsilon(\mathbf{r})]$ was chosen, and the topography was searched for by structural optimization. As a result, simulation of a $2 \times 2\ \mu\text{m}^2$ pattern with $\varepsilon_0 \approx 4.5 \times 10^{-5}$ gave topography and dimensions in perfect agreement with the experiments (Figure 3a,b). The agreement is the first indication suggesting that local expansion indeed is the driving force behind the observed structures.

The plateau formation can be understood simply in terms of increased surface area. Geometrical considerations provide an estimate for the height of a $L_0 \times L_0$ square pattern as

$$h(\varepsilon_0) = \sqrt{0.81\varepsilon_0 w(L_0 + 1.1 \times \text{fwhm})} \qquad (1)$$

where w is the edge width (see Supporting Information). We simulated the $2 \times 2\ \mu\text{m}^2$ pattern with expansions up to $\varepsilon_0 = 1\%$ and observed that eq 1 with $w \approx 3 \times \text{fwhm}$ captures well the dependence of height on strain (Figure 3c). Especially the square root dependence indicates how modest expansions are able to trigger notable structures. By inverting eq 1 and using the experimental data for $h(t)$, we could plot $\varepsilon_0(t)$, the expansion as a function of time (Supporting Information, Figure S4). The plot shows that strain grows linearly with irradiation time, here at rates around ∼0.01% per second.

The most plausible mechanism for the expansion mechanism is irradiation-induced defect formation. Raman spectra indicate that irradiation produces disordered regions (Figure 1e). It is reasonable to assume that, in the beginning of the process, isolated defects are formed. The density of isolated point defects can be estimated from the $I(\text{D})/I(\text{G})$ ratio.[24] Our nonirradiated CVD-grown graphene sample shows a ratio of ∼0.1, corresponding to an initial defect density $\sim 10^{11}\ \text{cm}^{-2}$ (Figure 1e).[24] Since the sharp D-band does not grow significantly in irradiation, the point defect density does not grow much beyond $\sim 10^{11}\ \text{cm}^{-2}$. Yet, because the lattice nevertheless expands, after the initial formation of scattered point defects, the expansion must be driven mainly by growth of isolated disordered regions. To investigate this possibility, we simulated mean lattice expansion due to repulsive point defects at various densities and strengths of influence (Figure 4a). Simulations show that $h \lesssim 20$ nm structures ($\varepsilon_0 \lesssim 0.01\%$) can be created by defect densities $\sim 10^{11}-10^{12}\ \text{cm}^{-2}$ and $h \approx 1$ nm structures ($\varepsilon_0 \sim 3 \times 10^{-5}\ \%$) by defect densities $\sim 10^{9}\ \text{cm}^{-2}$. This explains why elevated structures can be formed already at defect densities not visible in the Raman spectra.

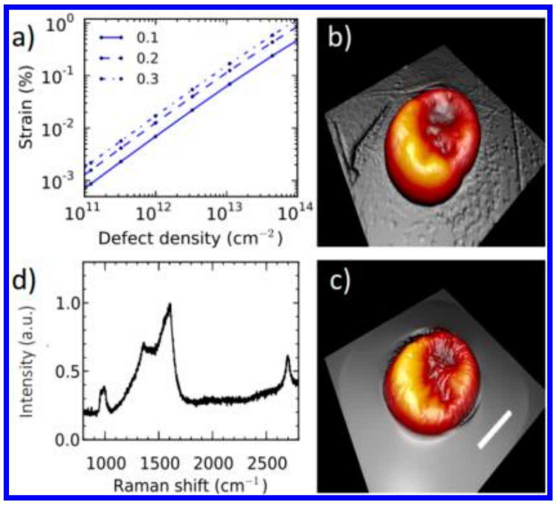

Figure 4. Point defects as the mechanism behind local expansion. (a) Averaged strain in graphene as a function of density of point defects, calculated using the elastic model with 2.5 Å grid spacing. The three different defect strengths of influence stand for the strain in the defected lattice point. (b) Experimentally observed, a 150 nm high partially collapsed structure resulting from prolonged irradiation at one spot. (c) Simulated and optimized structure corresponding to panel b ($\varepsilon_0 = 5\%$ within the structure). Vertical dimensions in b and c are scaled by a factor of 2; scale bar, 0.5 μm. (d) Raman spectrum of the collapsed structure.

The situation at longer irradiation times is different. Prolonged single spot irradiation created a ∼1.2-μm-diameter, 150-nm-high structure (Figure 4b). Measurement of the surface area indicated $\varepsilon_0 = 5\%$ expansion, assuming saturated expansion throughout the structure. Its stability was confirmed also in the simulation (Figure 4c). Most important, its Raman spectrum shows dominantly broad features, which is consistent with having highly disordered graphene (Figure 4d). Strains in the 5% range require defect densities above $10^{14}\ \text{cm}^{-2}$ (Figure 4a), which is in accordance with Raman spectra at high defect density.[24] At intermediate irradiations, the coexistence of normal and broad spectra can be understood by assuming that defects form preferentially in the vicinity of pre-existing defect regions that remain separated. As defect regions grow and finally coalesce at densities $\sim 10^{14}-10^{15}\ \text{cm}^{-2}$, the entire irradiated area becomes disordered and yields a completely broad Raman spectrum (see illustrative schematic in Supporting Information, Figure S5).

We lack direct evidence for the atomic structure of the defect, but let us consider one promising candidate—the bond rotation or Stone–Wales (SW) defect.[25] It is a fitting defect type because it requires no additional atoms, its formation energy of 4.6–5.7 eV[25] is close to the two-photon energy of 4–5 eV in experiments, and it causes expansion of suitable magnitude at suitable defect densities (Figure 4a and Supporting Information, Figure S6). Moreover, the SW defects have attractive interaction and can gradually develop into extended Haeckelite structures that consist of arrangements of pentagons, hexagons, and heptagons.[26,27] For example, the most stable Haeckelite, $\text{H}_{5,6,7}$, is 3% less dense than graphene, which is in rough agreement with the experimental saturation strain of 5% (Figure 4b).[28] Haeckelites are also metallic, which matches with the increased reflectance within the structures (Figure 1c).[27] While other mechanisms such as thin film interference could as well contribute to increased optical response,[29,30] SW defects and Haeckelite structures stand out as promising candidates to explain both increased reflectance and

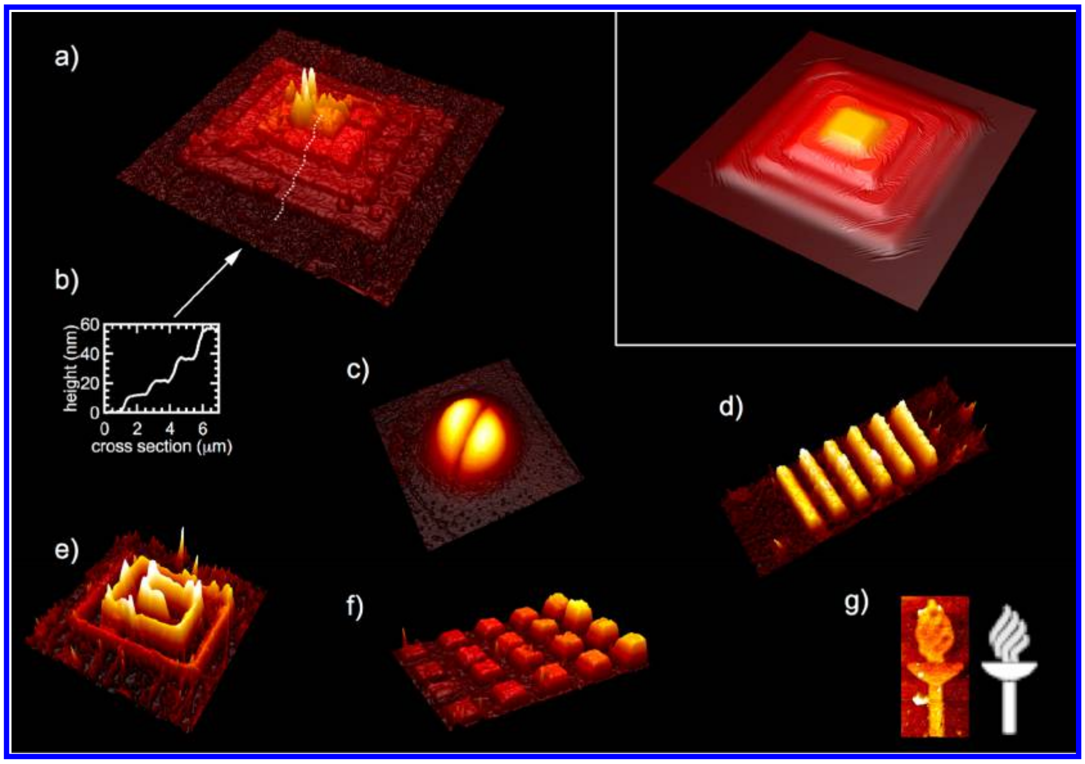

Figure 5. AFM images of 3D structures fabricated by direct laser writing. (a) Pyramid structure created by stepwise irradiation of levels. The field of view (FOV) is 17 × 17 μm^2. (b) Step profile along the dashed line in a. (c) 115 nm high semisphere which has collapsed symmetrically in the center. FOV is 1.8 × 1.8 μm^2. (d) Grating structure. FOV is 20 × 6.7 μm^2, and the maximum height is 25 nm. (e) Chiral structure with continuously increasing height. FOV is 8 × 8 μm^2, and the maximum height is 31 nm. (f) Matrix of squares. FOV is 19.8 × 14.7 μm^2, and the maximum height is 20 nm. (g) Torch with the bitmap image (on the right) used for direct laser writing. FOV is 3.5 × 7.4 μm^2, and the maximum height is 6 nm. Inset: Simulated pyramid structure with the same dimensions as in a. In the images the *z*-axis scale has been exaggerated to better visualize the structures.

lattice expansion, although confirmation requires further studies.

After establishing the method and mechanism for 3D patterning we describe fabrication of more complex 3D structures. The first example is a pyramid structure (Figure 5a). The pyramid was fabricated by first making the base level and then building the next levels stepwise (profile in Figure 5b). Such a pyramid was confirmed to be stable also in simulation (Figure 5, inset). The pyramid is a fascinating demonstration of the possibility to repeat the structure formation on a previously formed flat structure—such progressive control enables building arbitrarily complex architectures. In addition, we fabricated a 150 nm-high round semisphere, which had collapsed symmetrically, a miniature grating, a chiral structure (spiral), a matrix of squares, and a torch (Figures 5c−g).

The presented method for forging 2D graphene into 3D shapes opens exciting possibilities for further research. For example, shaping graphene into curved structures can be used to generate giant pseudomagnetic fields[5−7] or to control surface plasmon polaritons.[8] In addition, we propose that 3D structures of graphene can be used for fabricating scaffolds for layered materials, suspended device structures, and channel networks for nanofluidics, as well as optical and electronic devices. Finally, as the formation of 3D structures is simply based on lattice expansion, the presented concept is most likely generic to other 2D materials.

■ ASSOCIATED CONTENT

Ⓢ Supporting Information

The Supporting Information is available free of charge on the ACS Publications website at DOI: 10.1021/acs.nanolett.7b03530.

Additional materials and methods; details on elastic modeling; AFM, Raman and μm-XPS characterization data; and Figures S1−S6 (PDF)

■ AUTHOR INFORMATION

Corresponding Author

*E-mail: mika.j.pettersson@jyu.fi.

ORCID

Pasi Myllyperkiö: 0000-0003-1651-1676
Juha Koivistoinen: 0000-0002-7304-005X
Chia-Hao Chen: 0000-0003-1311-8342
Wei Yen Woon: 0000-0001-7299-9122
Mika Pettersson: 0000-0002-6880-2283

Author Contributions

A.J. and P.M. contributed equally to this work. M.P. planned the experiments, coordinated and supervised the work, and wrote the main part of the manuscript. A.J. planned the experiments and the sample fabrication and conducted AFM measurements and data analysis, as well as optical imaging. P.M. designed and developed the laser setups, performed most of the direct laser writing experiments, and did the data analysis. P. K. planned the simulations, wrote the computer codes, performed the simulations, did the data analysis, and wrote the computational part of the manuscript. J.A. built a part of the laser writing setup and performed initial laser writing experiments. J.K. and H.C.T. performed Raman measurements. V.M.H. and J.J.M. performed sample fabrication and characterization, including nanoindentation measurements and analysis. W.Y.W. planned and supervised XPS measurements and analysis, and wrote the XPS part of the manuscript. H.C.T., L.Y.C., and C.H.C. conducted XPS measurements and analysis. All of the authors discussed the results and commented on the manuscript.

Notes

The authors declare no competing financial interest.

■ ACKNOWLEDGMENTS

We thank Gerrit Groenhof for reading and commenting the manuscript and Kevin Roberts for help in sample fabrication. P.K. acknowledges the Academy of Finland for funding. W.Y.W. acknowledges funding from Ministry of Science and Technology of the Republic of China (MOST 106-2112-M-008-003-MY3).

■ REFERENCES

(1) Ferrari, A. C.; et al. *Nanoscale* **2015**, *7* (11), 4598−4810.
(2) Franklin, A. D. *Science* **2015**, *349* (6249), aab2750.
(3) Bao, Q.; Loh, K.-P. *ACS Nano* **2012**, *6* (5), 3677−3694.
(4) Deng, S.; Berry, V. *Mater. Today* **2016**, *19* (4), 197−212.
(5) Guinea, F.; Katsnelson, M. I.; Vozmediano, M. A. H. *Phys. Rev. B: Condens. Matter Mater. Phys.* **2008**, *77* (7), 075422.
(6) Guinea, F.; Katsnelson, M. I.; Geim, A. K. *Nat. Phys.* **2010**, *6* (1), 30−33.
(7) Levy, N.; Burke, S. A.; Meaker, K. L.; Panlasigui, M.; Zettl, A.; Guinea, F.; Castro Neto, A. H.; Crommie, M. F. *Science* **2010**, *329* (5991), 544−547.
(8) Smirnova, D.; Mousavi, S. H.; Wang, Z.; Kivshar, Y. S.; Khanikaev, A. B. *ACS Photonics* **2016**, *3* (5), 875−880.
(9) Bunch, J. S.; Verbridge, S. S.; Alden, J. S.; Van Der Zande, A. M.; Parpia, J. M.; Craighead, H. G.; Mceuen, P. L. *Nano Lett.* **2008**, *8* (8), 2458−2462.
(10) Lu, J.; Castro Neto, A. H.; Loh, K.-P. *Nat. Commun.* **2012**, *3*, 823.
(11) Boddeti, N. G.; Liu, X.; Long, R.; Xiao, J.; Bunch, J. S.; Dunn, M. L. *Nano Lett.* **2013**, *13* (12), 6216−6221.
(12) Blees, M. K.; Barnard, A. W.; Rose, P. A.; Roberts, S. P.; McGill, K. L.; Huang, P. Y.; Ruyack, A. R.; Kevek, J. W.; Kobrin, B.; Muller, D. A.; Mceuen, P. L. *Nature* **2015**, *524*, 204.
(13) Mu, J.; Hou, C.; Wang, H.; Li, Y.; Zhang, Q.; Zhu, M. *Science Advances* **2015**, *1* (10), e1500533−e1500533.
(14) Aumanen, J.; Johansson, A.; Koivistoinen, J.; Myllyperkiö, P.; Pettersson, M. *Nanoscale* **2015**, *7* (7), 2851−2855.
(15) Singh, G.; Rice, P.; Hurst, K. E.; Lehman, J. H.; Mahajan, R. L. *Appl. Phys. Lett.* **2007**, *91*, 033101.
(16) Ferrari, A. C.; Basko, D. M. *Nat. Nanotechnol.* **2013**, *8* (4), 235−246.
(17) Beams, R.; Cançado, L. G.; Novotny, L. *J. Phys.: Condens. Matter* **2015**, *27* (8), 083002.
(18) Koivistoinen, J.; Sládková, L.; Aumanen, J.; Koskinen, P.; Roberts, K.; Johansson, A.; Myllyperkiö, P.; Pettersson, M. *J. Phys. Chem. C* **2016**, *120* (39), 22330−22341.
(19) Johansson, A.; Tsai, H.-C.; Aumanen, J.; Koivistoinen, J.; Myllyperkiö, P.; Hung, Y.-Z.; Chuang, M.-C.; Chen, C.-H.; Woon, W. Y.; Pettersson, M. *Carbon* **2017**, *115*, 77−82.
(20) Farrokhi, H.; Zheng, H. Y.; Zhou, W.; Li, Z. L. *Opt. Express* **2012**, *20* (21), 23180−23185.
(21) Dong, T.; Sparkes, M.; Durkan, C.; O'Neill, W. *J. Laser Appl.* **2016**, *28* (2), 022202.
(22) Lee, C.; Wei, X.; Kysar, J. W.; Hone, J. *Science* **2008**, *321* (5887), 385−388.
(23) Rasool, H. I.; Ophus, C.; Klug, W. S.; Zettl, A.; Gimzewski, J. K. *Nat. Commun.* **2013**, *4*, 2811.
(24) Lucchese, M. M.; Stavale, F.; Ferreira, E. H. M.; Vilani, C.; Moutinho, M. V. O.; Capaz, R. B.; Achete, C. A.; Jorio, A. *Carbon* **2010**, *48* (5), 1592−1597.
(25) Ma, J.; Alfè, D.; Michaelides, A.; Wang, E. *Phys. Rev. B: Condens. Matter Mater. Phys.* **2009**, *80* (3), 033407.
(26) Openov, L. A.; Podlivaev, A. I. *Phys. Solid State* **2015**, *57* (7), 1477−1481.
(27) Terrones, H.; Terrones, M.; Hernández, E.; Grobert, N.; Charlier, J.-C.; Ajayan, P. M. *Phys. Rev. Lett.* **2000**, *84* (8), 1716−1719.
(28) Lusk, M. T.; Carr, L. D. *Phys. Rev. Lett.* **2008**, *100* (17), 175503.
(29) Cartamil-Bueno, S. J.; Steeneken, P. G.; Centeno, A.; Zurutuza, A.; van der Zant, H. S. J.; Houri, S. *Nano Lett.* **2016**, *16* (11), 6792−6796.
(30) Cartamil-Bueno, S. J.; Centeno, A.; Zurutuza, A.; Steeneken, P. G.; van der Zant, H. S. J.; Houri, S. *Nanoscale* **2017**, *9* (22), 7559−7564.